U. S. Naval Research Laboratory
Washington, DC 20375-5320

NRL/FR/6353--20-10,411

Effects of the Microstructural Grain Size and Aspect Ratio on the Mechanical Properties of Additively Manufactured Parts via Computational Analysis

Robert Saunders, Amit Bagchi
Multifunctional Materials Branch
Materials Science & Technology Division

Ajit Achuthan
Dept. of Mechanical and Aeronautical Engineering
Clarkson University

Athanasios P. Iliopoulos, John G. Michopoulos
Computational Multiphysics Systems Laboratory
Center of Materials Physics and Technology

April 22, 2021

REPORT DOCUMENTATION PAGE

Form Approved
OMB No. 0704-0188

1. REPORT DATE (DD-MM-YYYY)	2. REPORT TYPE	3. DATES COVERED (From – To)
22-04-2021	NRL Formal Report	May 2017 - August 2019

4. TITLE AND SUBTITLE

Effects of the Microstructural Grain Size and Aspect Ratio on the Mechanical Properties of Additively Manufactured Parts via Computational Analysis

5a. CONTRACT NUMBER

5b. GRANT NUMBER

5c. PROGRAM ELEMENT NUMBER
61153N

6. AUTHOR(S)

Robert Saunders, Ajit Achuthan, Athanasios Iliopoulos, John Michopoulos, Amit Bagchi

5d. PROJECT NUMBER

5e. TASK NUMBER

5f. WORK UNIT NUMBER
1G76

7. PERFORMING ORGANIZATION NAME(S) AND ADDRESS(ES)

U. S. Naval Research Laboratory
4555 Overlook Avenue, SW
Washington, DC 20375-5320

8. PERFORMING ORGANIZATION REPORT NUMBER

NRL/FR/6353--20-10,411

9. SPONSORING / MONITORING AGENCY NAME(S) AND ADDRESS(ES)

Office of Naval Research
One Liberty Center
875 N. Randolph Street, Suite 1425
Arlington, VA 22203-1995

10. SPONSOR / MONITOR'S ACRONYM(S)
ONR 6.1

11. SPONSOR / MONITOR'S REPORT NUMBER(S)

12. DISTRIBUTION / AVAILABILITY STATEMENT
Distribution A: Approved for public release; distribution is unlimited

13. SUPPLEMENTARY NOTES

14. ABSTRACT

Metal powder-based additive manufacturing (MPAM) methods can produce columnar grain microstructures that can vary greatly in size and aspect ratio (AR). This can significantly affect the mechanical properties of the resulting part. In an effort to link MPAM process parameters with the structural performance of the manufactured part, the effects of the grain structure on the constitutive response of the material must be determined. This work shows the development, implementation, and application of a microstructure-informed crystal plasticity constitutive model to describe the mechanical behavior of solidified material produced by MPAM. The model accounts for the presence and variability of grain size and AR associated with MPAM. Synthetic representative volume elements (RVEs) of MPAM-like microstructures from published literature are generated and converted into finite element models from which stress-strain behavior is extracted. Simulation results show that both the size and the AR of the grains have a significant effect on the yield strength and the initial strain hardening modulus.

15. SUBJECT TERMS
Metal Powder Additive Manufacturing, Microstructure, Mechanical Properties, Constitutive Behavior, Crystal Plasticity

16. SECURITY CLASSIFICATION OF:			17. LIMITATION OF ABSTRACT	18. NUMBER OF PAGES	19a. NAME OF RESPONSIBLE PERSON
a. REPORT	b. ABSTRACT	c. THIS PAGE			Robert Saunders
Unclassified Unlimited	Unclassified Unlimited	Unclassified Unlimited	SAR	41	19b. TELEPHONE NUMBER *(Include area code)* (202) 404-3489

Standard Form 298 (Rev. 8-98)
Prescribed by ANSI Std. Z39.18

This page intentionally left blank

CONTENTS

FIGURES

TABLES

This page intentionally left blank

EXECUTIVE SUMMARY

Metal powder-based additive manufacturing (MPAM) methods typically produce microstructures with a texture and columnar grain structure. The columnar grains can vary greatly in size and aspect ratio throughout the microstructure, which can affect the mechanical properties of the resulting part significantly. In an effort to link MPAM process parameters with the structural performance of the manufactured part, it is necessary to determine the effects of the grain structure on the constitutive response of the material.

In this report, the development of a microstructure-informed constitutive model to describe the mechanical behavior of the solidified material produced by the MPAM process is presented. The constitutive model is based on crystal plasticity and accounts for the presence and variability of grain size and aspect ratio of grain ensembles associated with the microstructural and poly-crystalline nature of metal alloys associated with MPAM. The crystal plasticity-based constitutive model captures the grain boundary effect by using a core-and-mantle grain configuration. This is done for the MPAM microstructure by considering a mapping of the columnar grains into idealized ellipsoidal domains. The details of the implementation of this approach are shown in this report. To apply the model, synthetic representative volume elements (RVEs) of MPAM microstructures are generated, via a continuum diffuse interface model, and are then segmented digitally into shape-preserving finite element models. Periodic boundary conditions are applied to the RVE and the resulting predicted stress-strain behavior is extracted.

Simulation results show that both the size and the aspect ratio of the grains have significant effects on the yield strength and the initial strain hardening modulus. By considering shape and aspect ratio effects, the predicted stress-strain behavior can differ by as much as 30% when not considering any geometric effects. Fitting statistical distributions to select results showed large stress concentrations in small and very elongated grains, indicating potential regions with a high probability of failure. The effect of the computed grain AR on yield strength and hardening modulus suggests that there is potential for tailoring the microstructure for optimal performance in terms of improved yield strength and hardening moduli when compared with those of conventionally manufactured materials.

This page intentionally left blank

EFFECTS OF THE MICROSTRUCTURAL GRAIN SIZE AND ASPECT RATIO ON THE MECHANICAL PROPERTIES OF ADDITIVELY MANUFACTURED PARTS VIA COMPUTATIONAL ANALYSIS

1. INTRODUCTION AND LITERATURE REVIEW

The microstructure of a part manufactured with a metal powder-based additive manufacturing (MPAM) process, such as selective laser melting (SLM), can be very different from that of a part manufactured using a conventional manufacturing process, such as casting and forming, for the same material. MPAM processes involve continued melting and solidification of a small amount of metallic powder along with remelting and solidification of previously deposited layers. The rate at which material cools after solidification, primarily determined by the thermal gradient, influences drastically the evolution of local microstructure and grain morphology. Since grain morphology affects mechanical properties significantly, the computational models for the structural analysis of a part made by MPAM require a constitutive model that can capture accurately the microstructural dependence of the material behavior. The present work proposes an advancement to a grain-size dependent crystal plasticity finite element (CPFE) model [2] to account for the effect of the columnar morphology of the grain's structure.

A brief literature review of columnar grains in MPAM and CPFE models is given first. Following that, the crystal plasticity constitutive model is presented, along with the methods used to homogenize and map the size and aspect ratio effects to the individual grains. Next, a continuum diffuse interface model is used to generate synthetic representative volume element (RVE) microstructures that represent features (*e.g.*, columnar grains) seen in MPAM-produced microstructures. These microstructure RVEs then are segmented digitally and are converted to FE models with periodic boundary conditions, which are used to compute and study the effects of aspect ratio (AR) and grain size. The anisotropy introduced by the microstructure also is examined by considering loading in the longitudinal (*i.e.*, along the dominant grain direction) and transverse (*i.e.*, out of plane of the dominant grain direction) directions.

1.1 Literature Review

1.1.1 Columnar Grain Structures in MPAM

In the MPAM processes, the continued melting and solidification involved in MPAM greatly influence the local microstructure. Furthermore, the microstructure of a multilayer build also is affected by the overlap of multiple scan tracks within a single layer along with the partial or full remelting of previously deposited layers [3]. A defining characteristic of the microstructure formed from the MPAM process is the presence of epitaxially grown columnar grains with different grain sizes and aspect ratios [4–12]. This texture typically occurs in cubic materials, where the $< 1\ 0\ 0 >$ crystal direction is the preferred growth direction. [13, 14] These microstructural morphologies have been observed with long vector scanning strategies and energy deposition beam power densities [3, 4, 6].

Manuscript approved April 22, 2021.

The < 1 0 0 > crystal direction has been reported to align at various angles with respect to the build and scan vectors of the AM part. For example, it has been reported [7] that a uniform < 1 0 0 > texture oriented at an angle of 60^o with the scan direction for unidirectional scanning is developed, and for bidirectional scanning, a < 1 0 0 > texture that started at 45^o with the scan direction in the first layer and then alternated the direction of the primary dendrites by 90^o between each layer. In some cases, a < 1 0 0 > cube texture has been reported rather than a fiber texture [3, 8]. As a consequence of the texture morphologies, varying mechanical properties have been observed in AM parts with strong fiber < 1 0 0 > textured microstructures, with a decrease of Young's modulus compared with non-textured AM microstructures [4]. Furthermore, elastic properties of AM parts can vary significantly depending on the orientation of the build direction with respect to the loading direction [14, 15]. AM materials with strong texture also are shown to have anisotropy in failure processes, such as fatigue crack growth [5].

Sometimes, AM microstructures that do not feature multilayer columnar grains and strong textures are characterized by grains that are elongated in the direction of the solid/liquid interface and the local thermal gradient during solidification. Consequently, the effects of the energy beam and the scan pattern used during manufacturing are apparent in the microstructure [16–18]. Occasionally, finer, more isotropic microstructures are produced by lower power densities and shorter vector scan patterns that change directions, such as in the case of island scanning [3, 19, 20]. Even when the whole microstructure does not have a significant globally dominating texture, local microtextures can still be present because of the cyclic thermal history seen during multilayer builds. Studies of several different scan patterns helped identify repeated localized bands of elongated grains with < 1 0 0 > texture when a global texture was not present [3].

A significant amount of work toward determining the mechanical behavior of AM metals can be identified, including the use of crystal plasticity simulations to model the effects of AM microstructures on the macroscopic properties and performance of the material. Several studies have utilized two-dimensional experimental or idealized microstructures [18, 21]. Few computational studies have utilized realistic, three-dimensional microstructures generated by simulations of the involved process. Examples of works that have used idealized three-dimensional microstructures representing AM relevant elongated grain aspect ratios and crystallographic textures can be found in [22, 23].

Another effort utilized 3D Cellular Automata to model the AM process and crystal plasticity simulations to simulate the spatial variation of microstructure and mechanical properties within a rectangular AM build [24]. In this study, the nucleation parameter used in the AM process simulation was varied to study the effect of grain size on response. Several experimental investigations also have studied variations within an AM build [25–28]. Finally, a recent study focuses on microstructure and property variation between disparate AM processes rather than spatial variation within a single build [29].

1.1.2 Grain Morphology Effect in CPFE

The core of any CPFE model is a crystal plasticity based constitutive model that captures heterogeneous deformation at a microscopic material length-scale by describing the elastic-plastic mechanical deformation at the level of slip systems [30]. Crystal plasticity-based constitutive models do not inherently have an intrinsic material length-scale in their classical formulation [30], and therefore cannot explain observed grain size dependence of some materials. However, efforts to develop microstructural feature size-dependent constitutive models have gained momentum over the past three decades due to the size-dependent material behavior observed in many experimental studies. One of the major focus areas of this effort was on introducing geometrically necessary dislocations (GNDs) into crystal plasticity constitutive models [31, 32].

Such formulations primarily rely on a strain gradient parameter that effectively captures the contribution of GNDs to the shear strength [33, 34]. A result of inclusion of the strain gradient parameter is that a length scale parameter associated with the microstructural feature dimensions emerges. This formulation also allows for the introduction of various mechanisms of material hardening by using Taylor's relation and expressing the plastic shear strain rate and shear strength relationships in terms of dislocation density.

The strain gradient-based formulation has taken a few different forms. In some studies, an approach following the framework of Cosserat-Koiter-Mindlin theories of higher order elasticity was followed [35–37]. While a number of strain gradient based models were phenomenological [33–35, 37–41], many directly introduced the strain gradient effects into the evolutionary laws of the internal slip system state variables [42–58].

Although the strain gradient-based size-dependent constitutive models have been successful in capturing the overall influence of microstructural features on flow stress, they also exhibited serious limitations; limitations that are fundamental and inherent to their formulation. One such limitation is the lack of an inherent mechanism to capture the yield stress variation as a function of grain size, the Hall-Petch relationship [59, 60]. In many models, this deficiency is addressed by enforcing a boundary region with preexisting GNDs [45, 47, 49, 54], while in others, it is addressed by explicitly introducing Hall-Petch models empirically into the formulations [61–63]. Another formulation by Lim *et al.* [60] used a two scale method, in which a meso-scale simulation (MSS) was used to redistribute the mobile part of the dislocation density within grains, consistent with the plastic strain. In addition to the inability to inherently capture the influence of grain boundaries on yield strength, the strain gradient-based constitutive models are mesh sensitive when implemented in a finite element framework [47]. Many models developed for ultragrain or nanograin materials, where dislocations glides are less important than discrete dislocation emissions from the grain boundary, do not rely on strain gradient formulations [64, 65]. Instead, these models follow various approaches to derive intrinsic material length-scales. For instance, Khan *et al.* [64] implemented speific deformation mechanisms explicitly in their model, while Yuan *et al.* followed a statistical approach [65].

Composite models are an alternative approach to strain gradient-based methods to introduce a characteristic length scale into the crystal plasticity-based constitutive models. The composite models operate by subdividing a grain into a core and a mantle [66–69]. The mantle, representing a region influenced by grain boundary, deforms differently than the core, which represents the inner volume of the grain. The characteristics of the core remain the same irrespective of the grain size. Therefore, in combination with the mantle, an inherent length-scale naturally emerges in the constitutive model. The emerged length-scale is a measure of the relative dominance of the grain boundary influence region on the overall behavior of the material. The composite model postulates that plastic flow occurs in localized zones of shear, as in slip bands, and these slip bands individually must generate an exceptional concentration of stress at the grain boundaries to propagate plastic flow throughout the material [70]. Meyers *et al.* [67] predicted an initial strengthening by using a work-hardened layer along the grain boundary in a polycrystalline aggregate. The flow stress of the grain aggregate is obtained from the average of the flow stress in the dislocation free grain interior region (core) and the grain boundary region (mantle). Fu *et al.* [71] advanced this model by allowing for the evolution of dislocation density in the mantle, subsequently advancing to the nanocrystalline regime [66] by accounting for the grain boundary rotation and slipping, thus capturing the reverse Hall-Petch effect. Grain size-dependent constitutive models on the core-and-mantle configuration also have been developed by coupling a single-crystal plasticity constitutive model with an appropriate cohesive interface model [68, 69]. Moghaddam *et al.* [72, 73] advanced the composite model by explicitly accounting for the increased resistance to dislocation nucleation and motion in grain boundary influence region. They used

the same strain-hardening rule of the crystal plasticity constitutive model to determine the increase in yield strength due to the grain boundary effect. Consequently, a change in the initial strain-hardening modulus also occurs due to the grain boundary effect. The model is also general, in the sense that it can capture the effect of any mechanisms of deformation arising from changes to the resistance (friction) to dislocation mobility as long as that resistance manifests an increase or decrease in yield strength with a corresponding decrease or increase in strain hardening. Unlike the strain gradient-based models, the core-and-mantle-based models can inherently capture the dependence of yield strength on grain size, and are relatively easy to implement.

While a large volume of literature is available on the effect of grain size on material properties, only a very few studies are reported on grain shape effects. This can be attributed to the fact that the grain structure is largely equiaxial in most of the conventional manufacturing processes, except forming and rolling. In the case of both of these exceptions, the literature available is focused on capturing the the grain shape effect during reforming or reshaping through direction grain deformation in the plastic regime, rather than in MPAM, where the directionality is primarily influenced by the thermal effects with little or no mechanical strain hardening. The gradient and curl of strains in strain gradient formulations treat elongated grains differently than equiaxed grains, thus producing a 'grain geometry' sensitivity [74]. To the authors knowledge, the only study that has followed a systematic approach to investigate the effect on columnar grain structures is Delannay *et al.* [48] for thin film application. However, with the wide use of additive manufacturing processes, modeling the effect of columnar grain structures is vital. An improved understanding of grain morphology effects on the properties of MPAM parts will aid in the development of process-structure-property linkages for creating truly tailored parts from the microscale to the macroscale.

2. THEORETICAL CONSIDERATIONS

Moghadham *et al.* [72, 73] formulated a crystal plasticity-based constitutive model that can capture grain boundary effect by using a core-and-mantle grain configuration. They captured grain size effect by considering a mapping of the equiaxial grains into idealized spherical domains, thus capturing the grain size effects. In the present work, this method is extened to MPAM microstructure by considering a mapping of the columnar grains into idealized ellipsoidal domains. This section begins by briefly presenting the basic formulation of the crystal plasticity constitutive model with grain boundary effect [72, 73]. Then, the formulation behind the mapping of columnar grains into idealized ellipsoidal domains is presented.

2.1 Crystal Plasticity Model with Grain Boundary Effect

The incremental formulation of plasticity theory is based on: (1) the evolution of Cauchy stress, $\boldsymbol{\sigma}$, defined on a Jaumann corotational frame of reference that rotates with the crystal lattice, $\boldsymbol{J}^*(\boldsymbol{\sigma})$, (2) the shear flow rate (slipping rate), $\dot{\gamma}^{(\alpha)}$, and (3) the strain hardening rate, $\dot{g}^{(\alpha)}$. The Cauchy stress evolution in the Jaumann corotational frame can be stated as

$$\boldsymbol{J}^*(\boldsymbol{\sigma}) + \boldsymbol{\sigma}(\boldsymbol{I} : \boldsymbol{D}^*) = \boldsymbol{C} : \boldsymbol{D}^*, \tag{1}$$

where $\boldsymbol{I}$ is the second order identity tensor, $\boldsymbol{D}^*$ is the elastic stretch rate tensor, and $\boldsymbol{C}$ is the tensor containing the material elastic constants.

The rate of slipping on a given slip system, α, is defined by the flow rule as

$$\dot{\gamma}^{(\alpha)}(t) = \dot{\gamma}^{(\alpha)}\left(\tau^{(\alpha)}(t), g^{(\alpha)}(t)\right), \tag{2}$$

where $\dot{\gamma}^{(\alpha)}(t)$ is the instantaneous rate of plastic shear strain on α at time t, and $\tau^{(\alpha)}(t)$ and $g^{(\alpha)}(t)$ are the resolved shear stress component and the shear strength, respectively, on α at that instance.

The accumulated plastic shear strain on α at time t is represented by

$$\gamma^{(\alpha)}(t) = \int_0^t \left|\dot{\gamma}^{(\alpha)}(t')\right| dt'. \tag{3}$$

The cumulative shear flow strain $\gamma(t)$, which is the total shear strain accumulated on all the slip systems at the material point until time t, can be determined as

$$\gamma(t) = \Sigma_{(\alpha)} \int_0^t \left|\dot{\gamma}^{(\alpha)}(t')\right| dt'. \tag{4}$$

A general form of a strength evolution rule can be expressed by defining an instantaneous rate of shear strength evolution, $\dot{g}^{(\alpha)}(t)$, on the slip system α as

$$\dot{g}^{(\alpha)}(t) = \dot{g}^{(\alpha)}(\gamma(t), \dot{\gamma}^{(\beta)}(t)), \tag{5}$$

where γ is the cumulative plastic shear strain on all the slip systems, and $\dot{\gamma}^{(\beta)}$ represents the instantaneous rates of shear flow in the individual slip systems, including α.

The increase in strength due to strain hardening as a result of mechanical loading of a slip system at the material point described by a position vector r can be stated as

$$g_L^{(\alpha)}(r,t) = \int_0^t \dot{g}^{(\alpha)}(t')dt', \tag{6}$$

Therefore, the instantaneous shear strength of the α slip system $g^{(\alpha)}$ can be expressed as

$$g^{(\alpha)}(r,t) = g_0(r) + g_L^{(\alpha)}(r,t), \tag{7}$$

where $g_0(r)$ represents the initial shear strength of the material at r before any plastic deformation due to loading begins to accumulate.

2.1.1 Grain Boundary Effect Formulation

The core-and-mantle configuration involves a grain that is considered to have two regions: a mantle region near its boundaries that has a higher resistance to dislocation nucleation, that represents a manifestation of the geometric constraint introduced by the grain boundary, and hence, called the grain boundary influence region, and the remaining core region that is sufficiently far away from the boundaries and is not influenced by them [72]. The resistance is maximum at the grain boundary, decreases with an increase in the distance from the grain boundary, and fades away at the inner boundary of the region. The thickness of the grain boundary influence region and the variation of resistance in this region are functions of interaction between the grains in that neighborhood, and hence may vary along the grain boundary. Accordingly, considering the annealed state of the material as the reference state, $g_0(r)$ is a material constant, $\tau_{0\infty}$, independent of the location in the core regions, while in the grain boundary influence region, it increases as the distance of the material point from the grain boundary decreases. Therefore, the instantaneous shear strength of the material points can be expressed as

$$g^{(\alpha)}(r,t) = \tau_{0\infty} + g_{GB}(r) + g_L^{(\alpha)}(r,t), \tag{8}$$

where the second term $g_{GB}(r)$ captures the increase in strength due to the grain boundary effect and assumes a value in the grain boundary influence region that vanishes towards the core.

An increase in strength that is associated with an increased resistance to dislocation motion, $g_{GB}(r)$, can be determined following the principle of crystal plasticity by considering an equivalent shear strain in a pre-processing step. To this end, a shear strain parameter, $\tilde{\gamma}_{GB}(s,\phi)$, is introduced, where s is the shortest distance of the material point from the nearest grain boundary and ϕ characterizes the nearest grain boundary. The symbol $\tilde{(\,)}$ is used to indicate that this is a mathematical quantity that simply enables us to introduce the physical quantity resistance in terms of a variation in strength and initial strain hardening modulus. With the introduction of this parameter, $g_{GB}^{(\alpha)}(r)$, can be expressed as

$$g_{GB}(r) = \int_0^{\tilde{\gamma}_{GB}(r)} \dot{g}^{(\alpha)}(\gamma) d\gamma. \tag{9}$$

For the numerical implementation, a linear form of the strain hardening equation is typically considered.

The special case of $sech^2$-type dependence between the strain-hardening modulus with total shear strain is introduced as follows:

$$h_{\alpha\beta} = q^{\alpha\beta} h_{0\infty} sech^2 \left| \frac{h_{0\infty}\gamma}{\tau_s - \tau_{0\infty}} \right|, \tag{10}$$

where $q^{\alpha\beta}$ differentiates latent hardening and self hardening, $h_{0\infty}$ is the initial hardening modulus, and τ_s is the maximum resistance to shear flow, g_{GB}^*. The instantaneous rate of shear strength can be written as

$$\dot{g}^{(\alpha)}(r,t) = \Sigma_{(\beta)} h_{\alpha\beta}(\gamma) \left| \dot{\gamma}^{(\beta)} \right|. \tag{11}$$

Equation (10) can be combined with Eq. (11) to obtain

$$\dot{g}^{(\alpha)} = h_{0\infty} sech^2 \left|K\gamma\right| \Sigma_{(\beta)} q^{\alpha\beta} \left|\dot{\gamma}^{(\beta)}\right|, \tag{12}$$

where $K = \frac{h_{0\infty}}{\tau_s - \tau_{0\infty}}$. Likewise, Eq. (9) can be written as

$$g_{GB}(r) = \frac{\tilde{h}_{0\infty}}{K}(tanh|K\tilde{\gamma}_{GB}|), \tag{13}$$

where $\tilde{h}_{0\infty}$ is given as

$$\tilde{h}_{0\infty} = h_{0\infty}\frac{(N_{ss} - 1)q + 1}{N_{ss}}, \tag{14}$$

where N_{ss} is the number of slip systems, q is the same as $q^{\alpha\beta}$ since it is the same for all the $(N_{ss} - 1)$ latent hardening slip systems, and it is equal to one for the self-hardening slip systems.

2.1.2 Grain Boundary Effect Homogenization

The material point implementation of the grain boundary effect in a computational analysis requires a precise spatial description of these parameters that is typically quite challenging for a realistic 3D crystallographic representation. An alternative approach is followed here to homogenize the grain boundary effect on an individual grain basis with the aid of a domain mapping of the given arbitrary grain geometry to a simple equivalent domain. A characteristic length scale parameter will emerge explicitly in the constitutive model as a consequence of the homogenization. The homogenized properties determined using simple geometric domains then are assigned to the corresponding grains of arbitrary geometry in the computational model.

The shear flow introduced to capture grain boundary effect can be homogenized by considering its average over the grain volume. We define the grain average equivalent shear flow strain as

$$\overline{\tilde{\gamma}_{GB}} = \frac{\int_{V_{GB}} \tilde{\gamma}_{GB}(r^*)dV}{V}. \tag{15}$$

Accordingly, the total strength and its rate of change can be stated respectively as

$$g^{(\alpha)}(r,t) = \tau_{o\infty} + \overline{g_{GB}} + \int_0^t \dot{g}^{(\alpha)}dt \tag{16}$$

and

$$\dot{g}^{(\alpha)} = \dot{g}^{(\alpha)}(\gamma + \overline{\tilde{\gamma}_{GB}}, \dot{\gamma}^{(\beta)}), \tag{17}$$

where $\overline{g_{GB}}$ (homogenized equivalent of Eq. (13)) is

$$\overline{g_{GB}} = \frac{\tilde{h}_{0\infty}}{K}(tanh|K\overline{\tilde{\gamma}_{GB}}|). \tag{18}$$

2.1.3 Ellipsoidal Domain Mapping

In order to perform the integration given by Eq. (15) analytically, each grain has to be mapped into a simple idealized geometry. Moghadham *et al.* [72] considered a spherical domain mapping, capturing the grain size effect. However, the spherical domain mapping is not capable of capturing the grain aspect ratio effect, and hence it is not appropriate for the columnar grains of the MPAM microstructure. Instead, we considered an ellipsoidal domain mapping, which can capture the aspect ratios seen in MPAM microstructures. Details of this mapping and integration are omitted here for brevity but can be found in Appendix A.

2.2 Microstructure Synthesis and Model

In this work, representative volume elements (RVEs) of microstructures that are based on those identified experimentally via imaging in actual MPAM microstructures [12] are synthesized using a continuum diffuse interface model [75, 76]. The details of the continuum diffuse interface model can be found in [76] and in Appendix B.

2.2.1 Segmentation

The resulting synthetic microstructure generated by the continuum diffuse interface model is represented in Fig. 1a. The data in the RVE is in the form of a 3D matrix with each (i, j, k) location containing a grain label from 1 to N, where N is the total number of distinct grains in the microstructure. The structure of this data is similar to the data structure used in grey-scale images such as those obtained from magnetic resonance imaging (MRI) and computed tomography (CT) scans. As such, the voxel image data is imported into ScanIP, a software developed by Simpleware (Synopsys, Mountain View, California, USA) to semi-automatically segment medical image data.

The segmentation process creates a surface representation of each grain, which is then used to generate a surface and a volume FE mesh. To eliminate the “stair stepping" effect inherent to the data structure, an algorithm to anti-alias and smooth the data is applied to ensure smooth contours along the grain boundaries. Following the smoothing of the surface data, the segmented boundaries are converted into a triangulated surface representation, then a multi-part surface decimation algorithm followed by a Delaunay tessellation with tetrahedral elements is applied [77]. A representative mesh used in this study is shown in Fig. 1b. A tetrahedral mesh is used in this work following the conclusions of [1, 78], where the tetrahedral mesh was shown to represent the grain geometries (and therefor overall RVE behavior) better at a similar or lower computational cost compared with a hexahedral mesh.

(a) RVE of synthetic microstructure generated by the 3-D continuum diffuse interface model

(b) Tetrahedral mesh of synthetic microstructure RVE of Fig. 1a

Fig. 1—Smoothed surface representation and tetrahedral mesh of an RVE [1]

2.3 FE Model Implementation

The FE model in this work is implemented in Abaqus/Standard (Dassault Systems, Providence, Rhode Island, USA) implicit FEA package [79], with the crystal plasticity constitutive model, implemented through a user material subroutine (UMAT). The tetrahedral elements used in this work are 10-noded serendipity tetrahedral elements (Abaqus designation C3D10) [80]. To test the model, we considered the uniaxial tensile loading of the material using an RVE. Periodic boundary conditions are enforced on all the external faces of the RVE. Applying periodic boundary conditions for unstructured mesh is not as straightforward as for the structured mesh because in an unstructured mesh, the nodal locations on the opposite face do not have a unique correspondence in terms of their relative locations on the faces. To circumvent the issue, we utilize the element interpolation functions to define the displacement of a desired point. For a 4-noded tetrahedral element, the element displacement, u, at any (x, y, z) location is defined as

$$u(x, y, z) = a_0 + a_1 x + a_2 y + a_3 z. \tag{19}$$

Now for any face, we select a node and define the corresponding point (x, y, z) on the opposite face using the same interpolation functions under isoparametric formulation. Accordingly, the value of the interpolation functions corresponding to the point on the opposite face can be determined by solving

$$\begin{bmatrix} 1 & x_1 & y_1 & z_1 \\ 1 & x_2 & y_2 & z_2 \\ 1 & x_3 & y_3 & z_3 \\ 1 & x_4 & y_4 & z_4 \end{bmatrix}^T \begin{bmatrix} a_0 \\ a_1 \\ a_2 \\ a_3 \end{bmatrix} = \begin{bmatrix} 1 \\ x \\ y \\ z \end{bmatrix}, \tag{20}$$

where x_i, y_i, and z_i are the coordinates of the four nodes of the current tetrahedral element. The solution to this equation provides the barycentric coordinates of the desired point within each element in the set. As per the definition of the interpolation functions, the solution to the preceding equation will only have all $a_i \geq 0$ if the point being searched for is contained within or on the surface of an element. It is possible that multiple

solutions exist, which occurs when the desired point is aligned exactly with an existing node or lies on the edge of two elements. When this occurs, any element with all $a_i \geq 0$ can be selected without any deleterious consequence because the interpolation functions of both elements result in the same value at that point. The process to apply this method to 10-node serendipity or 15-node quadratic tetrahedral elements is identical to that of the 4-node tetrahedral element.

3. RESULTS AND DISCUSSION

To evaluate the model, the effect of grain size and aspect ratio on mechanical properties was studied by comparing the predicted stress-strain behaviors under various loadings of samples with microstructures consisting of different average grain aspect ratios. Three RVE microstructures with different average grain aspect ratios were generated as shown in Fig. 2. Different aspect ratios were introduced by using three combinations of κ_0 and Δh in Eq. (B6). Three κ_0 values of 1, 3, and 5.5 were chosen to simulate an equiaxial grain structure such as that seen in the traditional manufacturing process, a slightly directionally biased grain structure, and a highly elongated grain structure, respectively. The latter two are representative of features that can be seen in MPAM microstructures. A convergence study on the number of grains and mesh density in the RVE was conducted. Comparison of stress-strain results demonstrated that any number of grains between 100 and ≈600 would be sufficient. The mesh density required to accurately represent 600 grains is what specified the upper limit. A middle ground was chosen such that each RVE has approximately 300 grains and dimensions of $0.15\,mm^3$. For convenience, each RVE will be referred to by the anisotropy factor κ_0 that controls the anisotropy associated with the grain aspect ratios. Crystallographic orientations for each grain were specified to be aligned with the axis of the fitted ellipsoid described in the previous section.

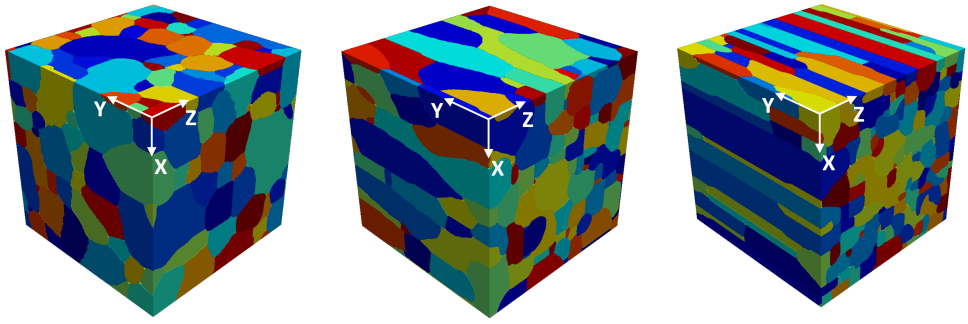

(a) $\kappa_0 = 1, \Delta h = 1$ (b) $\kappa_0 = 3, \Delta h = 0.6$ (c) $\kappa_0 = 5.5, \Delta h = 0.4$

Fig. 2—Synthetic microstructure RVEs generated by the continuum diffuse interface model with three combinations of κ_0 and Δh. [1]

Effective diameters and aspect ratios of each grain are obtained using the ellipsoid approximation of the grain geometry (Appendix A) for each of the generated RVEs and are shown in Fig. 3. From the figure, it can be seen that there is no significant variation in the grain size distribution between the RVEs (Fig. 3a). Having a nearly equal grain size distribution between the RVEs helps to isolate the aspect ratio effects during later analysis. The effective aspect ratios (Fig. 3b) show expected behavior as κ_0 values are changed. On average, an increase in κ_0 increases the aspect ratios seen. However, some higher aspect ratio grains are still present in the lower κ_0 cases. For instance, the highest grain aspect ratio in all the RVEs occurs in the $\kappa_0 = 3$ case and not in the 5.5 case.

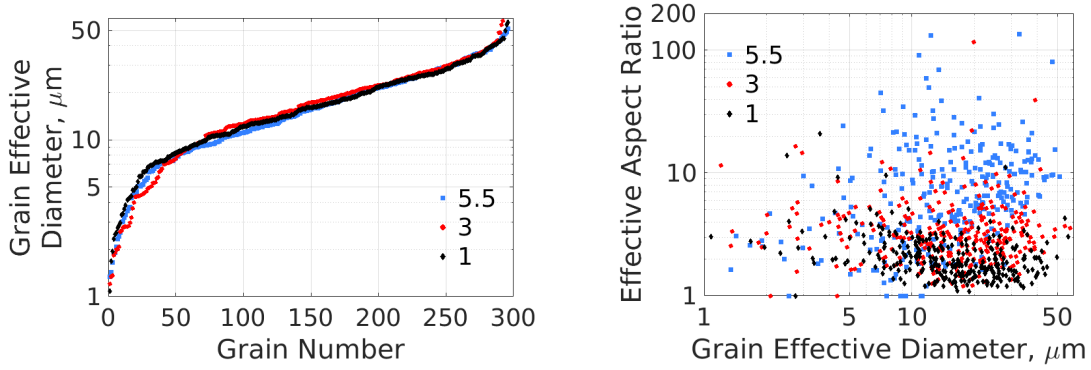

(a) Grain effective diameter (size) distribution sorted by size

(b) Effective grain aspect ratio (shape) compared to the effective grain diameters (size)

Fig. 3—Synthetic microstructure RVE grain size and shape distributions

In this work, 316L stainless steel is chosen as the material of interest in this work. The elastic material properties C_{11}, C_{12}, and C_{44} (Eq. (1)) are based on the work of [81, 82]. The following power law model is considered for the plastic strain flow rule $\dot{\gamma}^{(\alpha)} = \dot{a}\left(\frac{\tau^{(\alpha)}}{g^{(\alpha)}}\right)^{n}$. The plastic material parameters $\dot{a}$, n, and q (Eq. (14)) were obtained from [82]. The material properties $\tau_{0\infty}$, τ_s, $h_{0\infty}$ (Eq. (10)), and $\tilde{\gamma}^{*}_{GB}$ (Eq. (A10)) were determined by matching the stress-strain behavior of a grain-size dependent simulation with the stress-strain behavior reported in [83]. A simple trial-and-error approach along with a minimum mean square error criterion was adopted to obtain a set of values for these parameters. A grain boundary thickness δ_{GB} of 4.98 μm was chosen based on an average obtained using the experiment data of [84]. All the material parameters used in this study are shown in Table 1.

Table 1—Material Parameters Used for the Numerical Simulation

Parameters	Value
$\tau_{0\infty}$	75 MPa
τ_s	370 MPa
$\dot{a}$	0.001 /s
n	55
q	1
C_{11}	204.6 GPa
C_{12}	137.7 GPa
C_{44}	126.2 GPa
$\tilde{\gamma}^{*}_{GB}$	0.1
$h_{0\infty}$	330 MPa

3.0.1 MPAM Columnar Grain Effects on Initial Strength and Strain Hardening Modulii

The initial yield strength of individual grains as a function of grain size and grain aspect ratio can be calculated using Eq. (16) and is bounded between $\tau_{0\infty}$ and τ_s (Fig. 4). As grain size increases and/or as grain aspect ratio decreases to 1 (equiaxial), the grain boundary effect on yield strength diminishes and approaches $\tau_{0\infty}$. Conversely, the grain boundary effect in small and/or elongated grains causes the yield strength to

increase, approaching τ_s. In general, as κ_0, and therefore average aspect ratio, increases, more grains with a higher initial yield strength are seen as expected. These results indicate that elongated grains, such as those seen in MPAM microstructures and parts, will have a higher yield strength than the equiaxial grains observed in the traditionally manufactured parts.

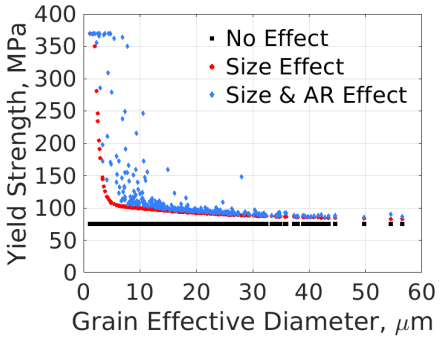

(a) $\kappa_0 = 1$

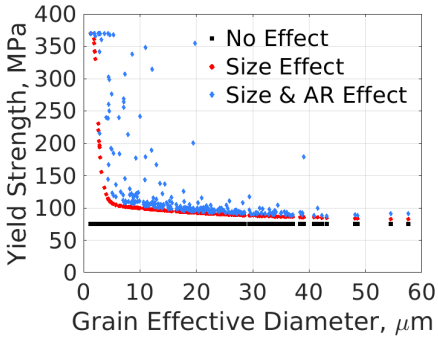

(b) $\kappa_0 = 3$

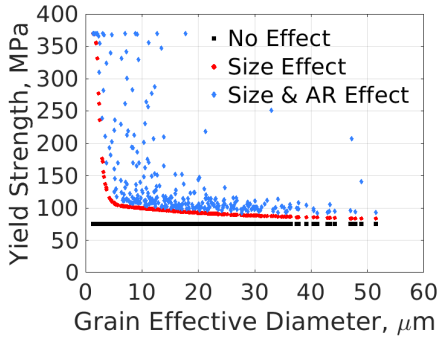

(c) $\kappa_0 = 5.5$

Fig. 4—Yield strength of every grain in each RVE with and without size and aspect ratio effects of the grains considered

The initial strain hardening modulus (Eq. (10)) can be calculated in the same manner as the yield strength to obtain the results shown in Fig. 5. In the case of initial strain hardening modulus, the maximum bound is $h_{0\infty}$, corresponding to large, equiaxial grains, and the minimum bound is zero, corresponding to smaller, elongated grains. The effect of the grain size and aspect ratio of the individual grains on their initial strain hardening modulus follows a similar trend as the grain yield strength. This is consistent with the strain hardening principle, *i.e.*, the strength and the strain hardening coefficients are inherently related to the increased resistance to dislocation nucleation. The grain boundary effect (Eq. (9)) is responsible for the relationship between the initial yield strength and the initial strain hardening coefficient.

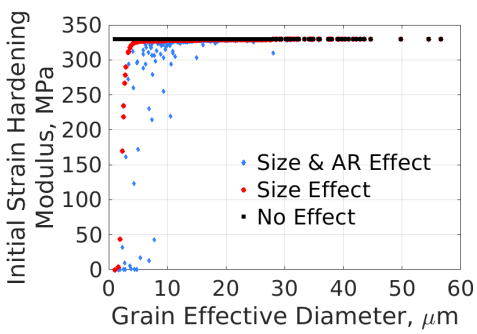

(a) $\kappa_0 = 1$

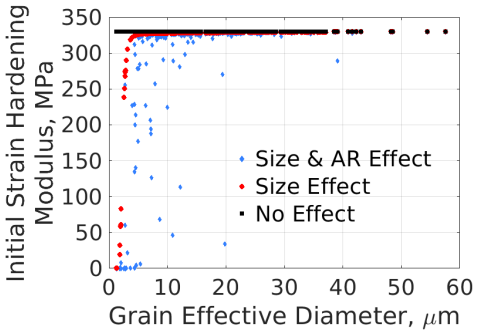

(b) $\kappa_0 = 3$

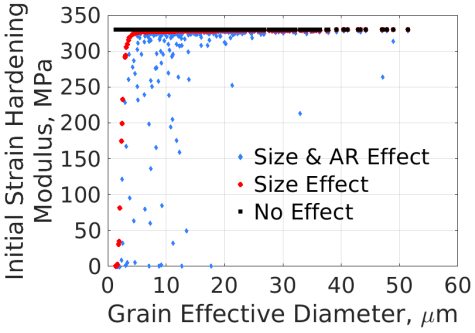

(c) $\kappa_0 = 5.5$

Fig. 5—Initial strain hardening modulus of every grain in each RVE with and without size and aspect ratio effects of the grains considered

3.0.2 Parametric Study on Mechanical Properties of Columnar Grains in MPAM

The stress-strain behaviors of the three synthetic MPAM RVEs were obtained under four different loading conditions: tension in the dominant grain direction (Y direction in Fig. 2), tension transverse to this direction (Z direction in Fig. 2), in-plane shear ($Y-Z$ direction in Fig. 2), and out-of-plane shear ($X-Z$ direction in Fig. 2). Here we have assumed that loading in the X and Z directions and shear in the $X-Y$ and $Y-Z$ planes produce nearly identical behavior. The loading is applied via a specified displacement to generate a volume-averaged nominal strain in the direction of the load of approximately 40%. The analysis results were post-processed by volume averaging the von Mises stress and equivalent plastic strain in the whole RVE and in each grain within the RVE.

The average stress-strain behaviors of the whole RVEs for different loading conditions are shown in Fig. 6. First, it is noted that utilizing no size or AR effects results in a behavior that is relatively constant as κ_0 is increased and the only significant differences in the behavior are due purely to the geometry and meshing of the models. The inclusion of only the size effect resulted in approximately a 10% higher stress at small strains with the difference diminishing as the plastic strain increased. These results were expected based on Figs. 4 and 5 where including the size effect increased the yield strength and decreased the strain hardening modulus slightly compared with the case without size or AR effects. Additionally, the inclusion of the size effect has a relatively constant effect on all three microstructures because the grain size distribution between the 3 RVEs is nearly identical, as mentioned earlier. Inclusion of aspect ratio (AR) into the model

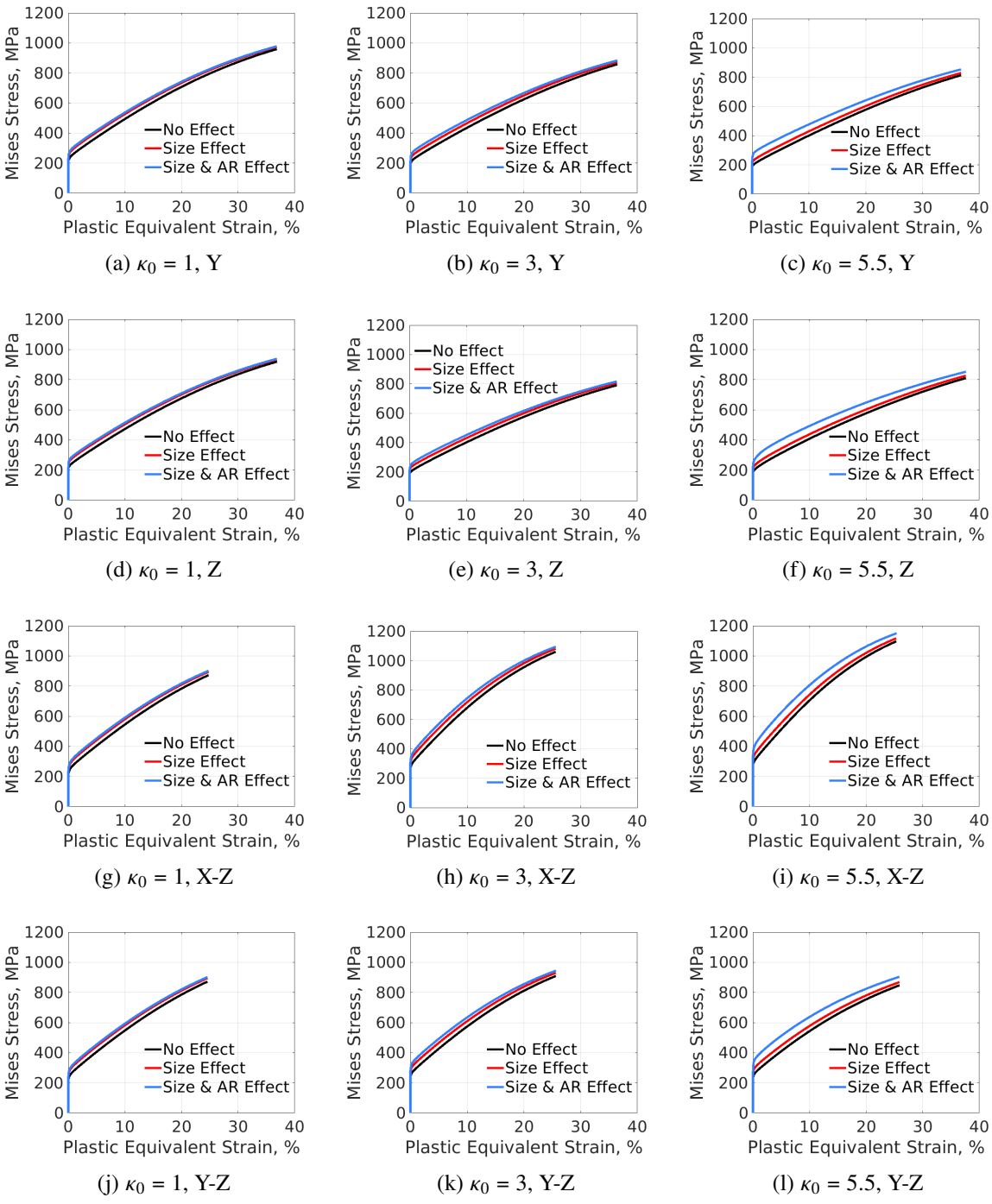

(a) $\kappa_0 = 1$, Y (b) $\kappa_0 = 3$, Y (c) $\kappa_0 = 5.5$, Y

(d) $\kappa_0 = 1$, Z (e) $\kappa_0 = 3$, Z (f) $\kappa_0 = 5.5$, Z

(g) $\kappa_0 = 1$, X-Z (h) $\kappa_0 = 3$, X-Z (i) $\kappa_0 = 5.5$, X-Z

(j) $\kappa_0 = 1$, Y-Z (k) $\kappa_0 = 3$, Y-Z (l) $\kappa_0 = 5.5$, Y-Z

Fig. 6—The average stress-strain behaviors of the whole RVEs for different loading conditions. From left to right, κ increases from 1 to 5.5. Each row corresponds to a different loading condition. Shape effect considerations have a constant effect on mechanical behavior in all cases, whereas a noticeable in increase can be seen for size and AR effects as κ increases.

amplified the effect, *i.e.*, the strength increased and the strain hardening modulus decreased further. In the most extreme instances (*e.g.*, Fig. 6l), an increase in stress at a given strain by more than 30% can be seen. It also can be seen that in the equiaxial ($\kappa_0 = 1$) microstructure the AR effect has almost no difference from the size effect. However, as the grains become more elongated to the levels seen in MPAM, the AR effect becomes very apparent and significantly alters the yield strength and the hardening behavior. These results demonstrate the need for consideration of both size and AR effects in MPAM microstructures where elongated grains, such as those in the $\kappa_0 = 5.5$ case, are not unusual.

In addition to the determination of RVE volume-averaged stress-strain behavior, the crystal plasticity models allow the accurate prediction of local stress and plastic strain fields within individual grains. By volume averaging over individual grains, distributions of stress as a function of strain can be found[1], which can provide insight for failure prediction. In following this distribution fitting procedure, the information in the 3D stress field quantities can be condensed into more interpretable stress-strain plots with quantile-based prediction intervals. An additional outcome of this fitting procedure is that the statistical distribution parameters (in this instance, the shape and scale of a gamma distribution) effectively become a function of strain, which could be used as a reduced-order representation of the whole RVE. Applying this procedure to a few cases of Fig. 6, using the gamma distribution median and interval containing 95% of the data, results in Figs. 7 and 8. In Figs. 7 and 8, wider variations in the distribution of the stress-strain can be used as a measure of the heterogeneity of stress-strain fields, and an indication of the interfacial stress concentrations and strain localizations around the grain boundaries. Excessively large stress and strain gradients could be an indication of early failure or reduced fatigue life.

For the case of loading in the Y direction (Fig. 7), the 95% intervals provide insight into the differences seen in the volume-averaged RVE response (Fig. 6). First, it is noted that the inclusion of grain boundary effects (SARE in the figure) results in a larger variance than the case without grain boundary effects (NE in the figure). This difference tends to diminish at large strains when the majority of grains have become saturated (*i.e.* reached τ_s). Next, it can be noted that, in all cases, the variance increases with stress. This can be thought of as the probability of stress concentrations increasing, leading to higher failure probabilities that one would expect at large plastic strains. Examining the equiaxial ($\kappa_0 = 1$) case compared with the MPAM elongated ($\kappa_0 = 5.5$) case, it can be seen that increase in variance with strain is greater in the equiaxial case than in the elongated case. The observed difference in variance increase with strain is believed to be due to the grain orientations, which are aligned with the elongated RVE, but have no preferred direction in equiaxial RVE. These preferred orientations mean that, in the elongated RVE, there is less crystallographic orientation mismatch between the grains, and therefore less heterogeneity locally. The heterogeneity, in turn, is likely causing activation of additional slip systems at higher strains, and thus is leading to a higher variance increase with strain in the equiaxial. Applying the principles stated, one could infer that a microstructure with elongated grains may exhibit larger heterogeneity in the stress and plastic strain fields at lower strains, while a microstructure with equiaxial grains is more likely to exhibit the heterogeneity at higher strains due to activation of multiple slip systems. These findings support what has been found in the literature that MPAM structures tend to have an increased yield strength but a higher probability of failing at lower strains (*i.e.* lower ductility). [85] Furthermore, the findings could only be obtained using a constitutive model that captured both the size and AR effects. Without such a model, the high variance at low strains would not be predictable in MPAM microstructures.

[1]The grain volume-averaging process generates a histogram of all grain stresses at each discrete strain value. Each histogram at each strain is then used to fit a statistical distribution using maximum likekihood estimation (MLE).

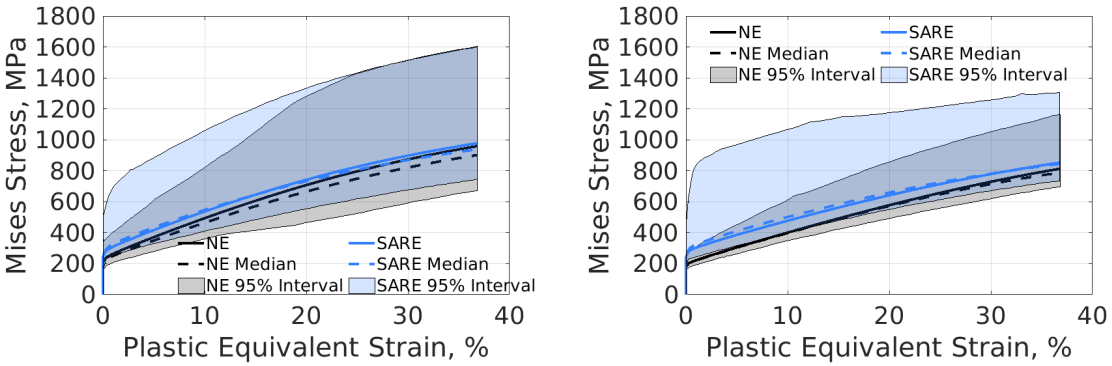

(a) $\kappa_0 = 1$ (b) $\kappa_0 = 5.5$

Fig. 7—Comparison of the distribution of volume-averaged stress in each grain for the no effect (NE) and size and aspect ratio effect (SARE) between the RVEs with κ_0 values of 1 and 5.5, loaded in the Y direction.

Many of the features seen in the Y loading case are also seen in the X-Z loading case of Fig. 8. The main difference here is that the MPAM elongated case appears to have a variance that increases more quickly than in the equiaxial case. In this instance, the result implies that the elongated case under shear loading is more likely to fail at low and high strains compared with the equiaxial case. This type of information can be utilized when designing for a given application with AM. If the load is expected to be of primarily one type (*e.g.*, shear, uniaxial, bending, *etc.*), then process parameters could be modified to produce a microstructure with grains oriented in a preferred direction, thus giving a higher yield strength and potentially higher ductility than conventional manufacturing processes.

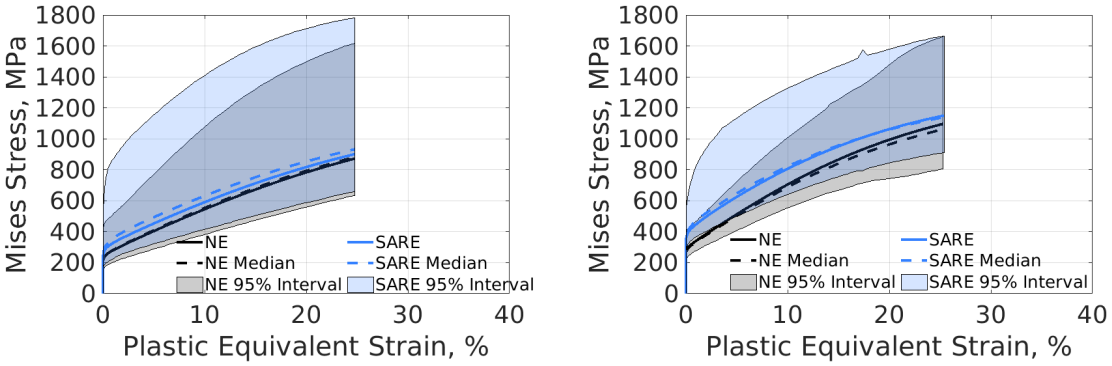

(a) $\kappa_0 = 1$ (b) $\kappa_0 = 5.5$

Fig. 8—Comparison of the distribution of volume-averaged stress in each grain for the no effect (NE) and size and aspect ratio effect (SARE) between the RVEs with κ_0 values of 1 and 5.5, loaded in the X-Z direction.

The results shown in Figs. 7 and 8 also reveal some remarkable features of the heterogeneity of the stress-strain behavior of individual grains. The median (dashed line) follows the RVE volume-averaged stress (thick solid line, curves from Fig. 6) closely. This indicates that there may be some potential to predict the RVE response from a smaller, but statistically equivalent domain. This approach would be similar to

what is done in the literature in constructing statistical volume elements (SVEs) [86, 87]. Additionally, there exists a potential to relate the gamma distribution parameters as a function of strain directly to the statistics of the RVE using machine learning, which gives the potential for nearly instantaneous stress-strain estimation and could link structure to properties during building of the MPAM part.

4. CONCLUSIONS

This paper has presented the development of a grain size- and aspect ratio-dependent crystal plasticity model or the high aspect ratio grains characteristic of metal powder additive manufacturing (MPAM) processes. The constitutive model was developed by applying a core-and-mantle approach in which the grain boundary influence region in the grain is treated as the mantle. After providing the model details in the most general form, we reduced it to a special case of a $sech^2$-type hardening, then further reduced it to a homogenized form mapped to a simple ellipsoidal domain. Synthetic microstructure representative volume elements (RVEs) were generated using a continuum diffuse interface model. RVEs of three different aspect ratios were generated based on published literature data on microstructures from MPAM processes for 316L stainless steel, and then were segmented and converted to finite element meshes. The FE models were analyzed in Abaqus/Standard with a crystal plasticity UMAT, periodic boundary conditions, and displacement loading. A parametric study was undertaken for simulating the responses of the three synthetic RVEs for four loading conditions with and without grain boundary effects. Grain boundary properties, such as the thickness of the mantle region and the effect of different materials, were not considered in this paper, and will be incorporated into this model in future research.

The results showed variations in stress-strain behavior as large as 30% for 316L stainless steel from MPAM processes with and without a grain boundary effect. The largest differences were in the cases that, on average, had the highest aspect ratios. Analysis of stress-strain behavior of the RVE using statistical distributions showed large stress concentrations within an RVE and that they could be related to failure probability. These results were consistent with those in the literature and predicted that microstructures with elongated grains such as those seen in MPAM, are more likely to have higher yield strengths but lower ductility and failure at lower strains.

The methodologies developed in this study are postulated to enable the construction of a machine learning model to modify MPAM process parameters *in situ*, and generate an optimal microstructure, with varying grain sizes and shapes, for a given application. Design of parts with an optimal microstructure could exhibit superior yield strength while maintaining a higher hardening modulus compared with traditionally manufactured microstructures. Likewise, process parameter optimization also could be carried out for different MPAM materials using the techniques discussed in this paper.

ACKNOWLEDGMENTS

We acknowledge the Sabbatical Faculty Fellowship with the Technology Management Training Group, Inc. (TMT Group), and support by US Naval Research Laboratory and Clarkson University for AA. Partial support for this project was provided by the Office of Naval Research (ONR) through the Naval Research Laboratory's Basic Research Program. This work was supported in part by a grant of computer time from the DOD High Performance Computing Modernization Program at the Air Force Research Laboratory (AFRL) DoD Supercomputing Resource Centers (DSRC).

REFERENCES

1. R. Saunders, A. Bagchi, and A. Achuthan, "A Method to Determine Local Stress Fields in Microstructure Features Produced by Additive Manufacturing," Proceedings of the Volume 2: Advanced Manufacturing, volume 2 (American Society of Mechanical Engineers, American Society of Mechanical Engineers), Nov 2017, pp. V002T02A025—-V002T02A025. ISBN 978-0-7918-5835-6, doi:10.1115/IMECE2017-71392. URL https://asmedigitalcollection.asme.org/IMECE/proceedings/IMECE2017/58356/Tampa,Florida,USA/265598.

2. R. Saunders, A. Achuthan, A. Iliopoulos, J. Michopoulos, and A. Bagchi, "Influence of grain size and shape on mechanical properties of metal Am materials," Proceedings of the 29th Annual Internation Solid Freeform Fabrication Symposium — An Additive Manufacturing Conference, 2018.

3. L. Thijs, K. Kempen, J. P. Kruth, and J. Van Humbeeck, "Fine-structured aluminium products with controllable texture by selective laser melting of pre-alloyed AlSi10Mg powder," *Acta Materialia* **61**(5), 1809 – 1819 (2013), ISSN 1359-6454, doi:https://doi.org/10.1016/j.actamat.2012.11.052. URL http://www.sciencedirect.com/science/article/pii/S1359645412008592.

4. T. Niendorf, S. Leuders, A. Riemer, H. A. Richard, T. Tröster, and D. Schwarze, "Highly anisotropic steel processed by selective laser melting," *Metallurgical and Materials Transactions B* **44**(4), 794–796 (2013).

5. A. Riemer, S. Leuders, M. Thöne, H. Richard, T. Tröster, and T. Niendorf, "On the fatigue crack growth behavior in 316L stainless steel manufactured by selective laser melting," *Engineering Fracture Mechanics* **120**, 15–25 (2014).

6. T. Niendorf, F. Brenne, and M. Schaper, "Lattice structures manufactured by SLM: on the effect of geometrical dimensions on microstructure evolution during processing," *Metallurgical and materials transactions B* **45**(4), 1181–1185 (2014).

7. H. Wei, J. Mazumder, and T. DebRoy, "Evolution of solidification texture during additive manufacturing," *Scientific Reports* **5**, 16446 (2015).

8. G. Dinda, A. Dasgupta, and J. Mazumder, "Texture control during laser deposition of nickel-based superalloy," *Scripta Materialia* **67**(5), 503–506 (2012).

9. I. Yadroitsev, P. Krakhmalev, I. Yadroitsava, S. Johansson, and I. Smurov, "Energy input effect on morphology and microstructure of selective laser melting single track from metallic powder," *Journal of Materials Processing Technology* **213**(4), 606–613 (2013).

10. K. Saeidi, X. Gao, Y. Zhong, and Z. J. Shen, "Hardened austenite steel with columnar sub-grain structure formed by laser melting," *Materials Science and Engineering: A* **625**, 221–229 (2015).

11. P. Kobryn and S. Semiatin, "The laser additive manufacture of Ti-6Al-4V," *JOM* **53**(9), 40–42 (2001).

12. A. J. Birnbaum, J. C. Steuben, E. J. Barrick, A. P. Iliopoulos, and J. G. Michopoulos, "Intrinsic strain aging, Σ3 boundaries, and origins of cellular substructure in additively manufactured 316L," *Additive Manufacturing* **29**(April), 100784 (Oct 2019), ISSN 22148604, doi:10.1016/j.addma.2019.100784. URL `https://doi.org/10.1016/j.addma.2019.100784https://linkinghub.elsevier.com/retrieve/pii/S2214860419303811`.

13. M. E. Glicksman, *Principles of solidification: an introduction to modern casting and crystal growth concepts* (Springer Science & Business Media, 2010).

14. S. Kou, *Welding Metallurgy*, 2nd ed. (John Wiley & Sons, Hoboken, New Jersey, 2002), ISBN 0-471-43491-4.

15. L. Hitzler, J. Hirsch, B. Heine, M. Merkel, W. Hall, and A. Öchsner, "On the anisotropic mechanical properties of selective laser-melted stainless steel," *Materials* **10**(10), 1136 (2017).

16. T. M. Rodgers, J. D. Madison, and V. Tikare, "Simulation of metal additive manufacturing microstructures using kinetic Monte Carlo," *Computational Materials Science* **135**, 78–89 (2017).

17. A. T. Polonsky, M. P. Echlin, W. C. Lenthe, R. R. Dehoff, M. M. Kirka, and T. M. Pollock, "Defects and 3D structural inhomogeneity in electron beam additively manufactured Inconel 718," *Materials Characterization* **143**, 171–181 (2018).

18. K. Kapoor, Y. S. J. Yoo, T. A. Book, J. P. Kacher, and M. D. Sangid, "Incorporating grain-level residual stresses and validating a crystal plasticity model of a two-phase Ti-6Al-4 V alloy produced via additive manufacturing," *Journal of the Mechanics and Physics of Solids* **121**, 447–462 (2018).

19. R. Casati, J. Lemke, and M. Vedani, "Microstructure and fracture behavior of 316L austenitic stainless steel produced by selective laser melting," *Journal of Materials Science & Technology* **32**(8), 738–744 (2016).

20. J. Suryawanshi, K. Prashanth, and U. Ramamurty, "Mechanical behavior of selective laser melted 316L stainless steel," *Materials Science and Engineering: A* **696**, 113–121 (2017).

21. M. B. Gorji, T. Tancogne-Dejean, and D. Mohr, "Heterogeneous random medium plasticity and fracture model of additively-manufactured Ti-6Al-4V," *Acta Materialia* **148**, 442–455 (2018).

22. W. Yan, S. Lin, O. L. Kafka, C. Yu, Z. Liu, Y. Lian, S. Wolff, J. Cao, G. J. Wagner, and W. K. Liu, "Modeling process-structure-property relationships for additive manufacturing," *Frontiers of Mechanical Engineering* **13**(4), 482–492 (2018).

23. A. Ahmadi, R. Mirzaeifar, N. S. Moghaddam, A. S. Turabi, H. E. Karaca, and M. Elahinia, "Effect of manufacturing parameters on mechanical properties of 316L stainless steel parts fabricated by selective laser melting: A computational framework," *Materials & Design* **112**, 328–338 (2016).

24. C. Herriott, X. Li, N. Kouraytem, V. Tari, W. Tan, B. Anglin, A. D. Rollett, and A. D. Spear, "A multi-scale, multi-physics modeling framework to predict spatial variation of properties in additive-manufactured metals," *Modelling and Simulation in Materials Science and Engineering* **27**(2), 025009 (2019).

25. J. J. Lewandowski and M. Seifi, "Metal additive manufacturing: a review of mechanical properties," *Annual Review of Materials Research* **46** (2016).

26. M. Seifi, A. Salem, D. Satko, J. Shaffer, and J. J. Lewandowski, "Defect distribution and microstructure heterogeneity effects on fracture resistance and fatigue behavior of EBM Ti–6Al–4V," *International Journal of Fatigue* **94**, 263–287 (2017).

27. T. R. Smith, J. D. Sugar, C. San Marchi, and J. M. Schoenung, "Strengthening mechanisms in directed energy deposited austenitic stainless steel," *Acta Materialia* **164**, 728–740 (2019).

28. K. L. Johnson, T. M. Rodgers, O. D. Underwood, J. D. Madison, K. R. Ford, S. R. Whetten, D. J. Dagel, and J. E. Bishop, "Simulation and experimental comparison of the thermo-mechanical history and 3D microstructure evolution of 304L stainless steel tubes manufactured using LENS," *Computational Mechanics* **61**(5), 559–574 (2018).

29. T. M. Rodgers, H. Lim, and J. A. Brown, "Three-Dimensional Additively Manufactured Microstructures and Their Mechanical Properties," *JOM* **72**(1), 75–82 (Jan 2020), ISSN 1543-1851, doi:10.1007/s11837-019-03808-x. URL `https://doi.org/10.1007/s11837-019-03808-x`.

30. D. Peirce, R. J. Asaro, and A. Needleman, "An analysis of nonuniform and localized deformation in ductile single crystals," *Acta Metallurgica* **30**(6), 1087–1119 (1982).

31. M. F. Ashby, "The deformation of plastically non-homogeneous materials," *The Philosophical Magazine: A Journal of Theoretical Experimental and Applied Physics* **21**(170), 399–424 (1970).

32. A. Arsenlis and D. M. Parks, "Crystallographic aspects of geometrically-necessary and statistically-stored dislocation density," *Acta Materialia* **47**(5), 1597–1611 (1999).

33. N. A. Fleck, G. M. Muller, M. F. Ashby, and J. W. Hutchinson, "Strain gradient plasticity: theory and experiment," *Acta Metallurgica et Materialia* **42**(2), 475–487 (1994).

34. J. W. Hutchinson and N. Fleck, "Strain gradient plasticity," *Advances in Applied Mechanics* **33**, 295–361 (1997).

35. N. A. Fleck and J. R. Willis, "A mathematical basis for strain-gradient plasticity theory. Part II: Tensorial plastic multiplier," *Journal of the Mechanics and Physics of Solids* **57**(7), 1045–1057 (2009).

36. N. M. Cordero, S. Forest, E. P. Busso, S. Berbenni, and M. Cherkaoui, "Grain size effects on plastic strain and dislocation density tensor fields in metal polycrystals," *Computational Materials Science* **52**(1), 7–13 (2012).

37. S. Forest, F. Barbe, and G. Cailletaud, "Cosserat modelling of size effects in the mechanical behaviour of polycrystals and multi-phase materials," *International Journal of Solids and Structures* **37**(46-47), 7105–7126 (2000).

38. U. Borg, "A strain gradient crystal plasticity analysis of grain size effects in polycrystals," *European Journal of Mechanics-A/Solids* **26**(2), 313–324 (2007).

39. M. Ekh, S. Bargmann, and M. Grymer, "Influence of grain boundary conditions on modeling of size-dependence in polycrystals," *Acta Mechanica* **218**(1-2), 103–113 (2011).

40. B. Klusemann, B. Svendsen, and H. Vehoff, "Modeling and simulation of deformation behavior, orientation gradient development and heterogeneous hardening in thin sheets with coarse texture," *International Journal of Plasticity* **50**, 109–126 (2013).

41. S. Wulfinghoff, E. Bayerschen, and T. Böhlke, "A gradient plasticity grain boundary yield theory," *International Journal of Plasticity* **51**, 33–46 (2013).

42. Y. Aoyagi and K. Shizawa, "Multiscale crystal plasticity modeling based on geometrically necessary crystal defects and simulation on fine-graining for polycrystal," *International Journal of Plasticity* **23**(6), 1022–1040 (2007).

43. Y. Aoyagi, T. Tsuru, and T. Shimokawa, "Crystal plasticity modeling and simulation considering the behavior of the dislocation source of ultrafine-grained metal," *International Journal of Plasticity* **55**, 43–57 (2014), ISSN 07496419, doi:10.1016/j.ijplas.2013.09.009. URL `http://dx.doi.org/10.1016/j.ijplas.2013.09.009`.

44. H. Askari, M. R. Maughan, N. Abdolrahim, D. Sagapuram, D. F. Bahr, and H. M. Zbib, "A stochastic crystal plasticity framework for deformation of micro-scale polycrystalline materials," *International Journal of Plasticity* **68**, 21–33 (2015).

45. E. P. Busso and K. S. Cheong, "Length scale effects on the macroscopic behaviour of single and polycrystalline FCC crystals," *Le Journal de Physique IV* **11**(PR5), Pr5—-161 (2001).

46. K. S. Cheong and E. P. Busso, "Discrete dislocation density modelling of single phase FCC polycrystal aggregates," *Acta Materialia* **52**(19), 5665–5675 (2004).

47. K. S. Cheong, E. P. Busso, and A. Arsenlis, "A study of microstructural length scale effects on the behaviour of FCC polycrystals using strain gradient concepts," *International Journal of Plasticity* **21**(9), 1797–1814 (2005).

48. L. Delannay and M. R. Barnett, "Modelling the combined effect of grain size and grain shape on plastic anisotropy of metals," *International journal of plasticity* **32**, 70–84 (2012).

49. L. P. Evers, D. M. Parks, W. A. M. Brekelmans, and M. G. D. Geers, "Crystal plasticity model with enhanced hardening by geometrically necessary dislocation accumulation," *Journal of the Mechanics and Physics of Solids* **50**(11), 2403–2424 (2002).

50. L. P. Evers, W. A. M. Brekelmans, and M. G. D. Geers, "Scale dependent crystal plasticity framework with dislocation density and grain boundary effects," *International Journal of Solids and Structures* **41**(18-19), 5209–5230 (2004).

51. M. G. D. Geers, W. A. M. Brekelmans, and P. J. M. Janssen, "Size effects in miniaturized polycrystalline FCC samples: strengthening versus weakening," *International Journal of Solids and Structures* **43**(24), 7304–7321 (2006).

52. J. Jiang, T. B. Britton, and A. J. Wilkinson, "The orientation and strain dependence of dislocation structure evolution in monotonically deformed polycrystalline copper," *International Journal of Plasticity* **69**, 102–117 (2015).

53. H. K. Lee, B. B. Jung, Y. D. Kim, W. B. Hwang, and H. C. Park, "Analysis of flow stress and size effect on polycrystalline metallic materials in tension," *Materials Science and Engineering: A* **527**(1-2), 339–343 (2009).

54. H. Lyu, A. Ruimi, and H. M. Zbib, "A dislocation-based model for deformation and size effect in multi-phase steels," *International Journal of Plasticity* **72**, 44–59 (2015).

55. F. T. Meissonnier, E. P. Busso, and N. P. O'Dowd, "Finite element implementation of a generalised non-local rate-dependent crystallographic formulation for finite strains," *International Journal of Plasticity* **17**(4), 601–640 (2001).

56. T. Ohashi, M. Kawamukai, and H. Zbib, "A multiscale approach for modeling scale-dependent yield stress in polycrystalline metals," *International Journal of Plasticity* **23**(5), 897–914 (2007).

57. T. Tinga, W. A. M. Brekelmans, and M. G. D. Geers, "Incorporating strain gradient effects in a multiscale constitutive framework for nickel-base superalloys," *Philosophical Magazine* **88**(30-32), 3793–3825 (2008).

58. H. Zhang and X. Dong, "Experimental and numerical studies of coupling size effects on material behaviors of polycrystalline metallic foils in microscale plastic deformation," *Materials Science and Engineering: A* **658**, 450–462 (2016).

59. L. P. Kubin and A. Mortensen, "Geometrically necessary dislocations and strain-gradient plasticity: a few critical issues," *Scripta Materialia* **48**(2), 119–125 (2003).

60. H. Lim, M. G. Lee, J. H. Kim, B. L. Adams, and R. H. Wagoner, "Simulation of polycrystal deformation with grain and grain boundary effects," *International Journal of Plasticity* **27**(9), 1328–1354 (2011).

61. G. Venkataramani, K. Kirane, and S. Ghosh, "Microstructural parameters affecting creep induced load shedding in Ti-6242 by a size dependent crystal plasticity FE model," *International Journal of Plasticity* **24**(3), 428–454 (2008).

62. D. Ozturk, A. Shahba, and S. Ghosh, "Crystal plasticity FE study of the effect of thermo-mechanical loading on fatigue crack nucleation in titanium alloys," *Fatigue & Fracture of Engineering Materials & Structures* **39**(6), 752–769 (2016).

63. S. Kotha, D. Ozturk, and S. Ghosh, "Parametrically homogenized constitutive models (PHCMs) from micromechanical crystal plasticity FE simulations, part I: Sensitivity analysis and parameter identification for Titanium alloys," *International Journal of Plasticity* **120**, 296–319 (Sep 2019), ISSN 07496419, doi:10.1016/j.ijplas.2019.05.008. URL `https://linkinghub.elsevier.com/retrieve/pii/S0749641919300622`.

64. A. S. Khan and J. Liu, "A deformation mechanism based crystal plasticity model of ultrafine-grained/nanocrystalline FCC polycrystals," *International Journal of Plasticity* **86**, 56–69 (2016), ISSN 07496419, doi:10.1016/j.ijplas.2016.08.001. URL `http://dx.doi.org/10.1016/j.ijplas.2016.08.001`.

65. R. Yuan, I. J. Beyerlein, and C. Zhou, "Emergence of grain-size effects in nanocrystalline metals from statistical activation of discrete dislocation sources," *Acta Materialia* **90**, 169–181 (2015), ISSN 13596454, doi:10.1016/j.actamat.2015.02.035. URL `http://dx.doi.org/10.1016/j.actamat.2015.02.035`.

66. H. H. Fu, D. J. Benson, and M. A. Meyers, "Computational description of nanocrystalline deformation based on crystal plasticity," *Acta Materialia* **52**(15), 4413–4425 (2004).

67. M. A. Meyersm and E. Ashworth, "A model for the effect of grain size on the yield stress of metals," *Philosophical Magazine A* **46**(5), 737–759 (1982).

68. Y. Wei, C. Su, and L. Anand, "A computational study of the mechanical behavior of nanocrystalline fcc metals," *Acta Materialia* **54**(12), 3177–3190 (2006).

69. Y. J. Wei and L. Anand, "Grain-boundary sliding and separation in polycrystalline metals: Application to nanocrystalline fcc metals," *Journal of the Mechanics and Physics of Solids* **52**(11), 2587–2616 (2004), doi:10.1016/j.jmps.2004.04.006.

70. R. W. Armstrong, I. Codd, R. M. Douthwaite, and N. J. Petch, "The plastic deformation of polycrystalline aggregates," *The Philosophical Magazine: A Journal of Theoretical Experimental and Applied Physics* **7**(73), 45–58 (1962).

71. H. H. Fu, D. J. Benson, and M. A. Meyers, "Analytical and computational description of effect of grain size on yield stress of metals," *Acta Materialia* **49**(13), 2567–2582 (2001).

72. M. G. Moghaddam, A. Achuthan, B. A. Bednarcyk, S. M. Arnold, and E. J. Pineda, "Development of a precipitate size-dependent crystal plasticity constitutive model for two-phase materials and its implementation on a multi-scale computational framework," *Materials Science and Engineering: A* **651**, 893–903 (2016), ISSN 0921-5093, doi:http://dx.doi.org/10.1016/j.msea.2015.11.042. URL //www.sciencedirect.com/science/article/pii/S0921509315306304.

73. M. Ghorbani Moghaddam, A. Achuthan, B. A. Bednarcyk, S. M. Arnold, E. J. Pineda, M. G. Moghaddam, A. Achuthan, B. A. Bednarcyk, S. M. Arnold, and E. J. Pineda, "Grain size-dependent crystal plasticity constitutive model for polycrystal materials," *Materials Science and Engineering: A* **703**(July), 521–532 (Aug 2017), ISSN 09215093, doi:10.1016/j.msea.2017.07.087. URL https://doi.org/10.1016/j.msea.2017.07.087https://linkinghub.elsevier.com/retrieve/pii/S0921509317309930.

74. J. C. Tucker, A. R. Cerrone III, A. R. Ingraffea, A. D. Rollett, A. R. Cerrone, A. R. Ingraffea, and A. D. Rollett, "Crystal plasticity finite element analysis for René88DT statistical volume element generation," *Modelling and Simulation in Materials Science and Engineering* **23**(3), 35003 (2015), ISSN 1361651X, doi:10.1088/0965-0393/23/3/035003. URL http://dx.doi.org/10.1088/0965-0393/23/3/035003.

75. D. Fan and L. Q. Chen, "Computer simulation of grain growth using a continuum field model," *Acta Materialia* **45**(2), 611–622 (1997), ISSN 1359-6454, doi:http://dx.doi.org/10.1016/S1359-6454(96)00200-5. URL http://www.sciencedirect.com/science/article/pii/S1359645496002005.

76. J. G. Michopoulos, A. P. Iliopoulos, J. C. Steuben, A. J. Birnbaum, Y. Fu, and J. H. Song, "Towards Computational Synthesis of Microstructural Crystalline Morphologies for Additive Manufacturing Applications," Proceedings of the Volume 1: 37th Computers and Information in Engineering Conference (American Society of Mechanical Engineers, American Society of Mechanical Engineers), Aug 2017, pp. V001T02A030———V001T02A030. ISBN 978-0-7918-5811-0, doi:10.1115/DETC2017-68149. URL https://asmedigitalcollection.asme.org/IDETC-CIE/proceedings/IDETC-CIE2017/58110/Cleveland,Ohio,USA/259126https://asmedigitalcollection.asme.org/IDETC-CIE/proceedings/IDETC-CIE2017/58110/Cleveland,Ohio,USA/259126.

77. P. G. Young, T. B. H. Beresford-West, S. R. L. Coward, B. Notarberardino, B. Walker, and A. Abdul-Aziz, "An efficient approach to converting three-dimensional image data into highly accurate computational models," *Philosophical Transactions of the Royal Society A: Mathematical, Physical and Engineering Sciences* **366**(1878), 3155–3173 (Sep 2008), ISSN 1364-503X, doi:10.1098/rsta.2008.0090. URL https://royalsocietypublishing.org/doi/10.1098/rsta.2008.0090.

78. I. Simonovski, L. Cizelj, and N. Jakšić, "The influence of finite element meshes on the results of a spatial polycrystalline aggregate model," *Nuclear Engineering and Design* **241**(4), 1184–1190 (2011), ISSN 00295493, doi:10.1016/j.nucengdes.2010.05.063.

79. Dassault Systèmes Simulia Corp., "Abaqus 2017, Theory, Benchmarks, and Examples Manuals," 2017.

80. K. T. Danielson, "Fifteen node tetrahedral elements for explicit methods in nonlinear solid dynamics," *Computer Methods in Applied Mechanics and Engineering* **272**, 160–180 (Apr 2014), ISSN 00457825, doi:10.1016/j.cma.2014.01.012. URL http://dx.doi.org/10.1016/j.cma.2014.01.012https://linkinghub.elsevier.com/retrieve/pii/S0045782514000255.

81. H. M. Ledbetter, "Monocrystal-Polycrystal Elastic Constants of a Stainless Steel," *Physica Status Solidi (a)* **85**(1), 89–96 (Sep 1984), ISSN 00318965, doi:10.1002/pssa.2210850111. URL http://doi.wiley.com/10.1002/pssa.2210850111.

82. I. Simonovski, K. F. Nilsson, and L. Cizelj, "Material Properties Calibration for 316L Steel Using Polycrystalline Model," Proceedings of the 13th International conference on nuclear engineering, 2005, p. 52. URL https://inis.iaea.org/search/search.aspx?orig{_}q=RN:38008188.

83. B. Kashyap and K. Tangri, "On the Hall-Petch relationship and substructural evolution in type 316L stainless steel," *Acta Metallurgica et Materialia* **43**(11), 3971–3981 (Nov 1995), ISSN 09567151, doi:10.1016/0956-7151(95)00110-H. URL https://linkinghub.elsevier.com/retrieve/pii/095671519500110H.

84. C. Tromas, J. C. Stinville, C. Templier, and P. Villechaise, "Hardness and elastic modulus gradients in plasma-nitrided 316L polycrystalline stainless steel investigated by nanoindentation tomography," *Acta Materialia* **60**(5), 1965–1973 (Mar 2012), ISSN 13596454, doi:10.1016/j.actamat.2011.12.012. URL https://linkinghub.elsevier.com/retrieve/pii/S1359645411008743.

85. J. Gale and A. Achuhan, "Application of ultrasonic peening during DMLS production of 316L stainless steel and its effect on material behavior," *Rapid Prototyping Journal* **23**(6), 1185–1194 (Oct 2017), ISSN 1355-2546, doi:10.1108/RPJ-09-2016-0140. URL https://www.emerald.com/insight/content/doi/10.1108/RPJ-09-2016-0140/full/html.

86. S. M. Qidwai, D. M. Turner, S. R. Niezgoda, A. C. Lewis, A. B. Geltmacher, D. J. Rowenhorst, and S. R. Kalidindi, "Estimating the response of polycrystalline materials using sets of weighted statistical volume elements," *Acta Materialia* **60**(13-14), 5284–5299 (Aug 2012), ISSN 13596454, doi:10.1016/j.actamat.2012.06.026. URL https://linkinghub.elsevier.com/retrieve/pii/S1359645412003989.

87. D. M. Turner and S. R. Kalidindi, "Statistical construction of 3-D microstructures from 2-D exemplars collected on oblique sections," *Acta Materialia* **102**, 136–148 (2016), ISSN 13596454, doi:10.1016/j.actamat.2015.09.011.

Appendix A

DOMAIN MAPPING AND SIMPLIFICATION

Let us consider a transformation of a grain with a given realistic geometry to a grain with a simple idealized geometry described by a smooth, convex surface $\psi(x, y, z) = k$. Let δ_{GB} be the constant thickness of the grain boundary influence region and $\tilde{\gamma}_{GB}(s)$ be the distribution of a plastic strain that would produce a resistance equivalent to the grain boundary resistance from its strain-hardening effect. Here, s is chosen as the distance from inner boundary of the grain boundary influence region along a direction that gives the shortest distance to the grain boundary (*i.e.*, normal to the grain outer boundary) such that $0 \leq s \leq \delta_{GB}$. A schematic representation of this concept is depicted in Fig. A1 for a point A on the intersection of the line AP with the circumference of an elliptical equivalent domain, representing the 2D cross-section of an ellipsoid associated with the source grain of the mapping.

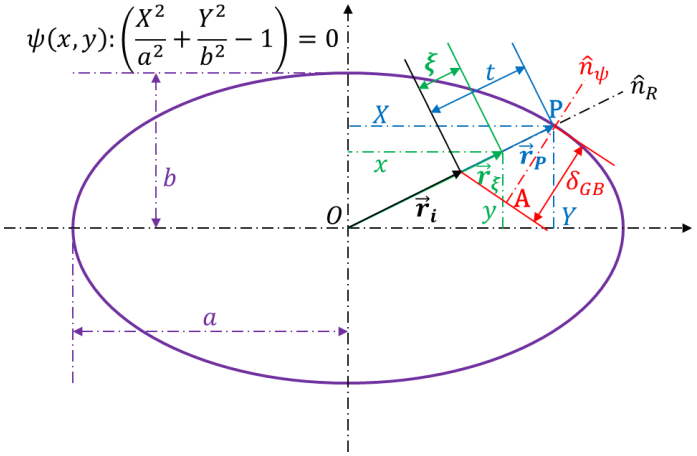

Fig. A1—2D illustration of the mapping of an arbitrary grain geometry to an ellipsoid.

Let us choose an arbitrary point with its position vector $\mathbf{r}_\xi$ that defines a material point inside the grain boundary influence region. Let $P(X, Y, Z)$ be a point on the outer surface of the grain boundary influence region along $\mathbf{r}_\xi$ with the position vector $\mathbf{r}_P$. Note that with P being on the grain boundary, X, Y, and Z are not arbitrary, but must satisfy the boundary conditions defined in the previous section. Let $\mathbf{r}_i$ be the position vector of a point on the inner boundary of the grain boundary influence region along $\mathbf{r}_\xi$. The thickness of the grain boundary layer along $\mathbf{r}_P$ can be related to the grain boundary layer thickness δ_{GB} by

$$(t\mathbf{n}_r) \cdot \mathbf{n}_\psi = \delta_{GB}, \tag{A1}$$

where t is the thickness of the grain boundary influence region at P along $\mathbf{r}_P$, which is equal to $\|\mathbf{r}_P - \mathbf{r}_i\|$, $\mathbf{n}_r$ is the normal vector along the position vector $\mathbf{r}_P$ and can be determined as

$$\mathbf{n}_r = \frac{1}{\sqrt{X^2 + Y^2 + Z^2}} \left(X\,\mathbf{i} + Y\,\mathbf{j} + Z\,\mathbf{k}\right), \tag{A2}$$

and $\mathbf{n}_\psi$ is a unit vector normal to ψ at P that can be defined as

$$\mathbf{n}_\psi(\mathbf{r}_P) = \frac{\nabla\psi_P}{\|\nabla\psi_P\|}. \tag{A3}$$

Rearranging Eq. (A1), we obtain

$$t = \frac{\delta_{GB}}{\mathbf{n}_r \cdot \mathbf{n}_\psi}, \tag{A4}$$

To determine $\tilde{\gamma}_{GB}(s)$ at $\mathbf{r}_\xi$, the quantities ξ and s are related in a similar manner to obtain

$$\xi = \frac{s}{\mathbf{n}_r \cdot \mathbf{n}_\psi}. \tag{A5}$$

The position vector $\mathbf{r}_\xi$ now can be written in terms of $\mathbf{r}_P$ and δ_{GB} according to

$$\begin{aligned} \mathbf{r}_\xi &= \mathbf{r}_i + \xi\mathbf{n}_r \\ &= \mathbf{r}_P - (t-\xi)\,\mathbf{n}_r \\ &= \mathbf{r}_P - \frac{(\delta_{GB}-s)\mathbf{n}_r}{\mathbf{n}_r \cdot \mathbf{n}_\psi}. \end{aligned} \tag{A6}$$

Therefore, s corresponding to a location $\mathbf{r}_\xi$ in terms of grain boundary description ψ at $P(X,Y,Z)$ can be obtained as

$$s = \delta_{GB} - \left\|\mathbf{r}_P - \mathbf{r}_\xi\right\| \mathbf{n}_r \cdot \mathbf{n}_\psi. \tag{A7}$$

Thus, the distribution of $\tilde{\gamma}_{GB}(s)$ for the range of $\xi \in \{0, t\}$ defined by the position vector $\mathbf{r}_\xi$ corresponding to the location $P(X,Y,Z)$ now can be determined by substituting the corresponding values of s as

$$\begin{aligned} \tilde{\gamma}_{GB}(s) &= \tilde{\gamma}_{GB}(\delta_{GB} - \left\|\mathbf{r}_P - \mathbf{r}_\xi\right\| \mathbf{n}_r \cdot \mathbf{n}_\psi) \\ &= \tilde{\gamma}_{GB}\left(\left(\left\|\mathbf{r}_\xi\right\| - \|\mathbf{r}_i\|\right) \mathbf{n}_r \cdot \mathbf{n}_\psi\right). \end{aligned} \tag{A8}$$

Integration over the mapped grain volume dV (Eq. (15)) is performed in two steps, first along radial incremental length dr and then along tangential incremental surface $r^2\,sin(\phi)\,d\theta\,d\phi$, according to

$$\overline{\tilde{\gamma}_{GB}} = \frac{8}{V}\int_0^{\pi/2}\int_0^{\pi/2}\int_{r_i}^{r_P} \tilde{\gamma}_{GB}(r,\theta,\phi) r^2 sin(\phi) dr d\theta d\phi. \tag{A9}$$

The actual distribution of $\overline{\tilde{\gamma}_{GB}}$ should be known in order to obtain a closed-form analytical solution. Here, we use a linear profile along the radial direction as an approximation to the actual distribution, allowing the integration in the radial dimension $\tilde{\gamma}_{GB}(s) = Cs$, where $C = \frac{\tilde{\gamma}^*_{GB}}{\delta_{GB}}$, to be performed. This assumption yields

$$\begin{aligned} \tilde{\gamma}_{GB} &= Cs \\ &= C\left(\left\|\mathbf{r}_\xi\right\| - \|\mathbf{r}_i\|\right)\mathbf{n}_r \cdot \mathbf{n}_\psi. \end{aligned} \tag{A10}$$

Noting that $\left\|\mathbf{r}_\xi\right\| = r$ enables expressing integration as

$$\overline{\tilde{\gamma}_{GB}} = \frac{8C}{V}\int_0^{\pi/2}\int_0^{\pi/2}\left(-\|\mathbf{r}_i\|\frac{\|\mathbf{r}_P\|^3 - \|\mathbf{r}_i\|^3}{3} + \frac{\|\mathbf{r}_P\|^4 - \|\mathbf{r}_i\|^4}{4}\right)\mathbf{n}_r \cdot \mathbf{n}_\psi sin(\phi)d\theta d\phi. \tag{A11}$$

Taking advantage of the relationships between r_P and r_i (Eq. (A6)) enables representing the homogenized grain boundary shear flow strain as

$$\overline{\tilde{\gamma}_{GB}} = \frac{8C}{V}\left(I_1 + I_2 + I_3\right), \tag{A12}$$

where

$$I_1 = \frac{1}{2}\int_0^{\pi/2}\int_0^{\pi/2}\|\mathbf{r}_P\|^2\left(\frac{\delta_{GB}}{\mathbf{n}_r \cdot \mathbf{n}_\psi}\right)^2 sin(\phi)d\theta d\phi, \tag{A13}$$

$$I_2 = -\frac{1}{3}\int_0^{\pi/2}\int_0^{\pi/2}\|\mathbf{r}_P\|\left(\frac{\delta_{GB}}{\mathbf{n}_r \cdot \mathbf{n}_\psi}\right)^3 sin(\phi)d\theta d\phi, \tag{A14}$$

$$I_3 = \frac{1}{12}\int_0^{\pi/2}\int_0^{\pi/2}\left(\frac{\delta_{GB}}{\mathbf{n}_r \cdot \mathbf{n}_\psi}\right)^4 sin(\phi)d\theta d\phi. \tag{A15}$$

The above expressions can be simplified further by considering a general quadric surface with $\psi(x, y, z) = 0$, where

$$\psi(x, y, z) = A_1x^2 + A_2y^2 + A_3z^2 + A_4xy + A_5yz + A_6xz + A_7x + A_8y + A_9z + A_{10}. \tag{A16}$$

Individual grains then are mapped to a domain that is optimal in terms of minimum linear least square (llsq) error, satisfying the volume equivalence constraint by enforcing $\sum_{i=1}^{3} A_i = a\ constant$. It should be noted that the three radii of the ellipsoid correspond to A_1, A_2, and A_3. The three radii of the ellipsoid also are used

to determine the effective aspect ratio of the ellipsoid as $A_1/(A_2 + A_3)$. For its implementation, Eq. (A16) is first rearranged to the form

$$\begin{aligned}\psi(x,y,z) = x^2+y^2+z^2-B_1\left(x^2+y^2-2z^2\right)-B_2\left(x^2-2y^2+z^2\right)-2B_3xy-2B_4yz-2B_5xz-B_6x-B_7y-B_8z-B_9 \\ = 0,\end{aligned} \tag{A17}$$

where B_i are simple linear combinations of A_i. The solution to the llsq problem, which provides the coefficients of Eq. (A17), is given as

$$B_i = \left(C_{ik}C_{km}\right)^{-1} C_{mj}d_j, \tag{A18}$$

where B is a $[9 \times 1]$ vector containing the coefficients, d is an $[N \times 1]$ vector, and N is the number of data points corresponding to the locations describing the grain surface. Each component of the vector d is equal to $x^2 + y^2 + z^2$ at a given location. C is an $[N \times 9]$ matrix with each column corresponding to an individual location defining the grain surface as

$$\left[\ \left(x^2+y^2-2z^2\right), \left(x^2-2y^2+z^2\right), 2xy, 2yz, 2xz, x, y, z, 1\ \right]. \tag{A19}$$

From the definition of an ellipsoid, we know that for $r = 1$, the magnitude of $\mathbf{r}_P$ can be expressed as

$$\|\mathbf{r}_P\| = \frac{1}{\sqrt{\left(\frac{C_\theta S_\phi}{A_1}\right)^2 + \left(\frac{S_\theta S_\phi}{A_2}\right)^2 + \left(\frac{C_\phi}{A_3}\right)^2}} \tag{A20}$$

and

$$\mathbf{r}_P = \|\mathbf{r}_P\|\left(C_\theta S_\phi \hat{i} + S_\theta S_\phi \hat{j} + C_\phi \hat{k}\right). \tag{A21}$$

From this, we obtain the normal vector along $\mathbf{r}_P$ (Eq. (A2)) as

$$\begin{aligned}\mathbf{n}_r &= \frac{\mathbf{r}_P}{\|\mathbf{r}_P\|} \\ &= C_\theta S_\phi \hat{i} + S_\theta S_\phi \hat{j} + C_\phi \hat{k}.\end{aligned} \tag{A22}$$

Likewise, $\mathbf{n}_\psi$ is found using Eq. (A3) as

$$\mathbf{n}_\psi(\mathbf{r}_P) = \frac{\frac{C_\theta S_\phi}{A_1^2}\hat{i} + \frac{S_\theta S_\phi}{A_2^2}\hat{j} + \frac{C_\phi}{A_3^2}\hat{k}}{\sqrt{\left(\frac{C_\theta S_\phi}{A_1^2}\right)^2 + \left(\frac{S_\theta S_\phi}{A_2^2}\right)^2 + \left(\frac{C_\phi}{A_3^2}\right)^2}}. \tag{A23}$$

The scalar product $\mathbf{n}_r \cdot \mathbf{n}_\psi$ then is calculated by taking the inner product of the expressions in Eqs. (A22) and (A23) as

$$\mathbf{n}_r \cdot \mathbf{n}_\psi = \frac{\left(\frac{C_\theta S_\phi}{A_1}\right)^2 + \left(\frac{S_\theta S_\phi}{A_2}\right)^2 + \left(\frac{C_\phi}{A_3}\right)^2}{\sqrt{\left(\frac{C_\theta S_\phi}{A_1^2}\right)^2 + \left(\frac{S_\theta S_\phi}{A_2^2}\right)^2 + \left(\frac{C_\phi}{A_3^2}\right)^2}}. \tag{A24}$$

Equations (A20) and (A24) can be inserted into Eq. (A15) and integrated to establish $\overline{\tilde{\gamma}_{GB}}$. It is now trivial to see that all the equations derived for the ellipsoidal domain mapping degenerate to the spherical domain mapping under the conditions $A_1 = A_2 = A_3 = d/2$, thus capturing only the grain-size effect of a microstructure with equiaxial grains.

This page intentionally left blank

Appendix B

CONTINUUM DIFFUSE INTERFACE MODEL

The continuum diffuse interface model for simulating grain evolution within 3D domains was first introduced in [B75] for 2D domains and without aspect ratio control capability. In the present case, the framework has been generalized for 3D domains and parameters for controlling the size and aspect ratio variation distributions have been introduced. In the diffuse-interface field model, an arbitrary polycrystalline microstructure is described by a set of continuous field variables η_i $(i = 1, ..., p)$ that are called orientation field variables for distinguishing different orientations of grains with p being the number of possible grain orientations.

It is assumed that across the grain boundaries between the grain η_1 and its neighbors, the value of η_1 changes continuously from 1 to 0. The total free energy of an inhomogeneous system in terms of all the orientation field variables and their gradients is expressed as

$$F = \int [\ f_0\ (\ \eta_1(r), \eta_2(r), ..., \eta_p(r)\ ) + \sum_{i=n}^{p} \frac{\boldsymbol{\kappa}_i}{2} (\nabla \eta_i(r))^2\ ]\, d^3r, \tag{B1}$$

where f_0 is the local free energy density, which is a function of field variables η_i, and $\boldsymbol{\kappa}_i$ are the gradient energy coefficients that, in general, are tensors reflecting the crystal symmetry or gradient directional bias of the η_is. The main requirement for f_0 is that it has p degenerate minima with equal depth f_{min} located at

$$(\ \eta_1(r), \eta_2(r), ..., \eta_p(r)\ ) = (1, 0, ..., 0), (0, 1, ..., 0), ..., (0, 0, ..., 1) \tag{B2}$$

in p-dimensional space.

Because the orientation field variables are non-conserved quantities, their local evolution rates can be considered linearly proportional to the variational derivative of the total free energy with respect to the local orientation field variable, and therefore, they are governed by the Ginzburg–Landau equations,

$$\begin{aligned} \frac{\partial \eta_i(r,t)}{\partial t} &= -L_i \frac{\delta F}{\delta \eta_i(r,t)},\ \ i \\ &= 1, 2, ..., p, \end{aligned} \tag{B3}$$

where L_i are relaxation coefficients, t is time, and F is total free energy. Substitution of the free energy form in Eq. (B1) into Eq. (B3) leads to the form

$$\frac{\partial \eta_i(r,t)}{\partial t} = -L_i[\frac{\delta f_0(\eta_i)}{\eta_i} - \boldsymbol{\kappa}_i \nabla^2 \eta_i], i = 1, 2, ..., p. \tag{B4}$$

By following the process described in [B75] by specifying the initial free energy, we can finally derive the system of equations that need to be solved for obtaining the evolution of all η_i in the form

$$\frac{\partial \eta_i}{\partial t} = -L_i[-a_1\eta_i + a_2\eta_i^3 + 2a_3\eta_i \sum_{j\neq i}^{p} \eta_j^2 - \boldsymbol{\kappa}_i \nabla^2 \eta_i], \tag{B5}$$

for $i = 1, 2, ..., p$ and for $a_k, (k = 1, 2, 3)$ being positive definite constants that can be defined as indicated in [B75] to have the values $a_1 = a_2 = 1,\ a_3 = a_1/2$.

To simulate the grain growth evolution for the purpose of generating synthetic RVE microstructures, the set of kinetic equations (Eq. (B5)) are to be solved numerically by discretizing them in space and time. Prior to presenting the discrete forms, we present a simplification for the second-order diagonal tensors $\boldsymbol{\kappa}_i$. The components of this coefficient can be thought of as expressing the proportion of discrepancy of the gradient energy coefficients along directions x and y relative to those along z. This generalization can be expressed by $\boldsymbol{\kappa}_i = ((\kappa_{0x}\kappa_i, 0, 0), (0, \kappa_{0y}\kappa_i, 0), (0, 0, \kappa_i))$. For the case in which we want to allow the response to be the same on both directions in the $x - y$ plane, we can set $\kappa_0 = \kappa_{0x} = \kappa_{0y}$, and this is the case that we will use for our numerical analysis in this paper.

Based on these considerations, the Laplacian is discretized by the following finite difference discrete form

$$\begin{aligned}\nabla^2\eta_i = \frac{1}{3(\Delta h)^2} [\ \kappa_0 (\ &-\eta_i(x,y,z) + \eta_i(x-\Delta h,y,z) + \eta_i(x+\Delta h,y,z) \\ &+ \eta_i(x,y-\Delta h,z) + \eta_i(x,y+\Delta h,z) + \eta_i(x,y,z-\Delta h) + \eta_i(x,y,z+\Delta h)\ )\ ],\end{aligned} \tag{B6}$$

where Δh is the size of the grid element and κ_0 represents a factor representing the bias acting on the $x - y$ plane such that we can tune a desired variation of grain anisotropy aspect ratio relative to the z-direction.

The discretization with respect to time, was implemented via a simple explicit integration Euler scheme described by

$$\eta_i(t + \Delta t) = \eta_i(t) + \frac{d\eta_i}{dt}\Delta t, \tag{B7}$$

where Δt represents the integration time step. Thus, for a given initial distribution of η_i, which describes the initial grain structure, the temporal and spatial evolution of the microstructure can be obtained by solving Eq. (B5) numerically via Eqs. (B6) and (B7).